Supplement of

Why Did Ozone Rise During Shanghai's Static Management? A Statistical and Radical Chemistry Perspective

Jian Zhu[1], Shanshan Wang[1,2], Chuanqi Gu[1], Zhiwen Jiang[1], Sanbao Zhang[1], Ruibin Xue[1], Yuhao Yan[1], Bin Zhou[1,2,3]

[1]Shanghai Key Laboratory of Atmospheric Particle Pollution and Prevention (LAP[3]), Department of Environmental Science and Engineering, Fudan University, Shanghai, 200433, China.

[2]Institute of Eco-Chongming (IEC), Shanghai, 202162, China.

[3]Institute of Atmospheric Sciences, Fudan University, Shanghai, 200433, China.

Corresponding to: Bin Zhou (binzhou@fudan.edu.cn) and Shanshan Wang (shanshanwang@fudan.edu.cn)

Text S1 meteorological conditions.

We evaluated whether there were significant changes in ground-level airflows in Shanghai during the static management period compared to the same periods in 2020 and 2021. An analysis of the frequency distribution of wind speed and wind direction (see Figure S7a-S7f) during the lockdown period shows that wind speeds were primarily distributed in the range of 2-4 m s^{-1}, with the predominant wind direction between 0-180° (with 0° as true north and counting clockwise). Compared to the same periods in 2020 and 2021, during the 2022 lockdown period, there was an increase in the frequency of northerly winds and a decrease in the frequency of westerly winds. This indicates that Shanghai was upwind of other cities in the Yangtze River Delta region for most of the time during the static management period in 2022. From the mean diurnal profiles of wind speed and wind direction, it can be observed that during the lockdown period, the predominant wind direction throughout the day was between 90-150°, and higher wind speeds typically occurred in the afternoon, corresponding to a wind direction of around 100°.

From the rose diagrams of ozone and its precursors NO_2 and VOCs (see Figure S8), during the 2022 lockdown period, the predominant winds during high ozone levels were southerly winds with higher wind speeds and westerly winds with lower wind speeds. When NO_2 concentrations were high, wind speeds were generally lower, and the predominant wind direction during periods of high VOCs concentrations was southwest to south. Comparing the same period in 2020 and 2021, it is obvious that the transmission contribution of ozone and its precursors from other cities in the Yangtze River Delta in 2022 was limited.

We also analyzed the percentage change in meteorological conditions in Shanghai and its surrounding areas during the 2022 lockdown period compared to the same periods in 2020 and 2021 as shown in Figure S9 and Figure S10. The results indicate that in 2022, the 2-m temperature and relative humidity in the Shanghai area showed a slight decrease compared to 2020 and 2021, with the changes being relatively small. surface net solar radiation in 2022 decreased compared to 2020 but was slightly higher than in 2021, while total precipitation in 2022 was significantly higher than in 2020. During the static management period in Shanghai, the decrease in average temperature, weakening of solar radiation, and increased precipitation may have contributed to the reduction in O_3 production by slowing down chemical reaction rates. ERA5 reanalysis data also indicates that during the static management period, there were minimal variations in 2-meter temperature, relative humidity, surface net solar radiation, boundary layer height, and total cloud cover in the Shanghai area, whereas these parameters exhibited more significant changes in the surrounding regions. The above results indicate that the increase in O_3 concentration in Shanghai during the 2022 static management period was not due to changes in meteorological conditions.

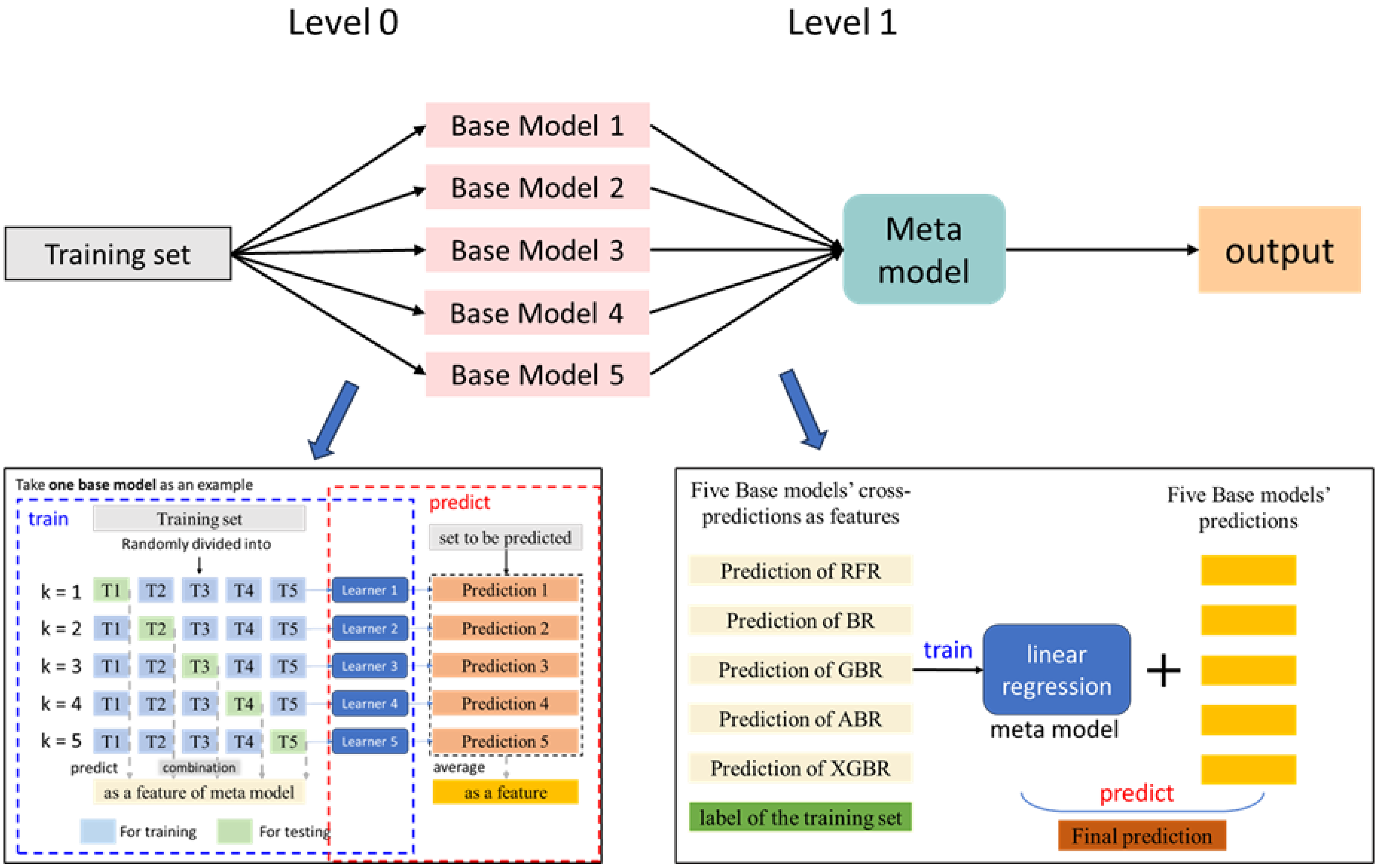

Figure S1. Framework of the stacking model.

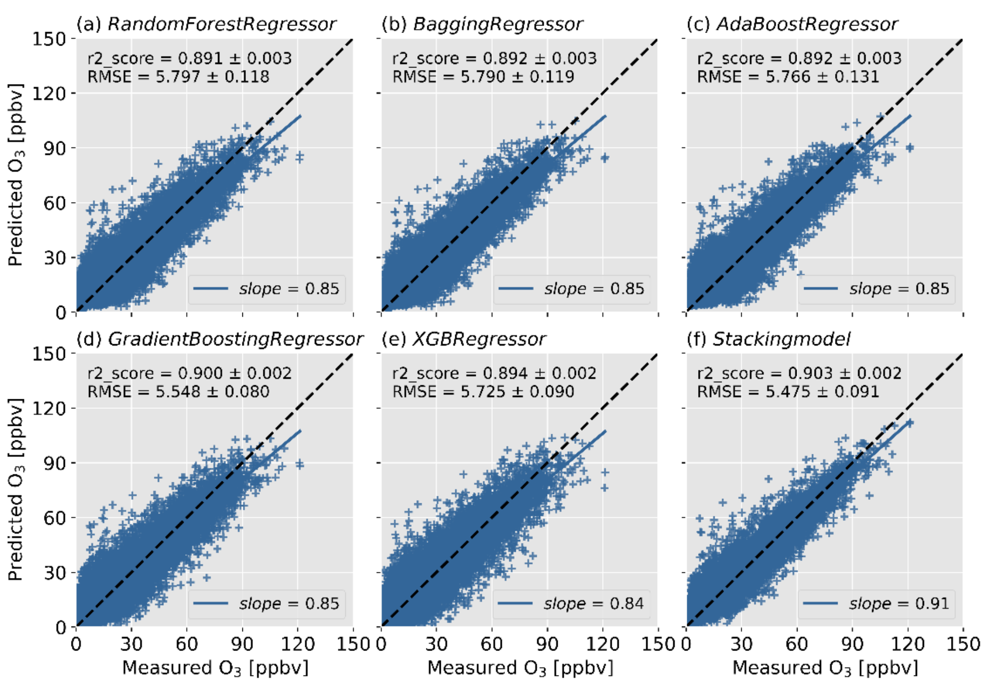

Figure S2. Performance comparisons of the stacking model and the five base models after 5-fold cross-validation with the indicators of the coefficient of determination (r2_score), root mean square error (RMSE), and slope between predicted and measured O_3.

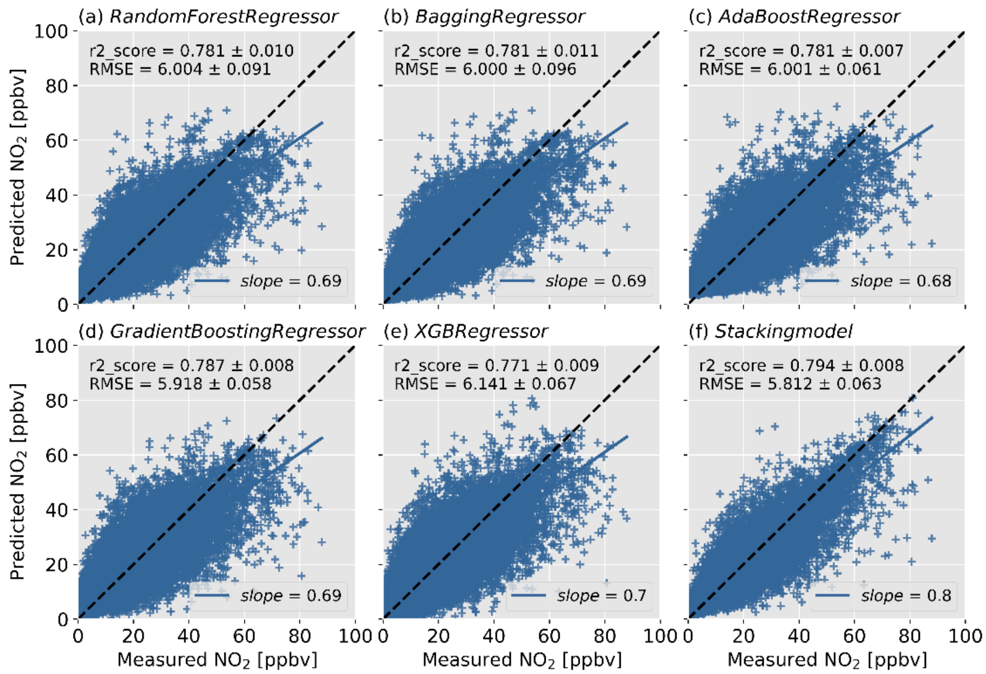

Figure S3. Performance comparisons of the stacking model and the five base models after 5-fold cross-validation with the indicators of r2_score, RMSE, and slope between predicted and measured NO_2.

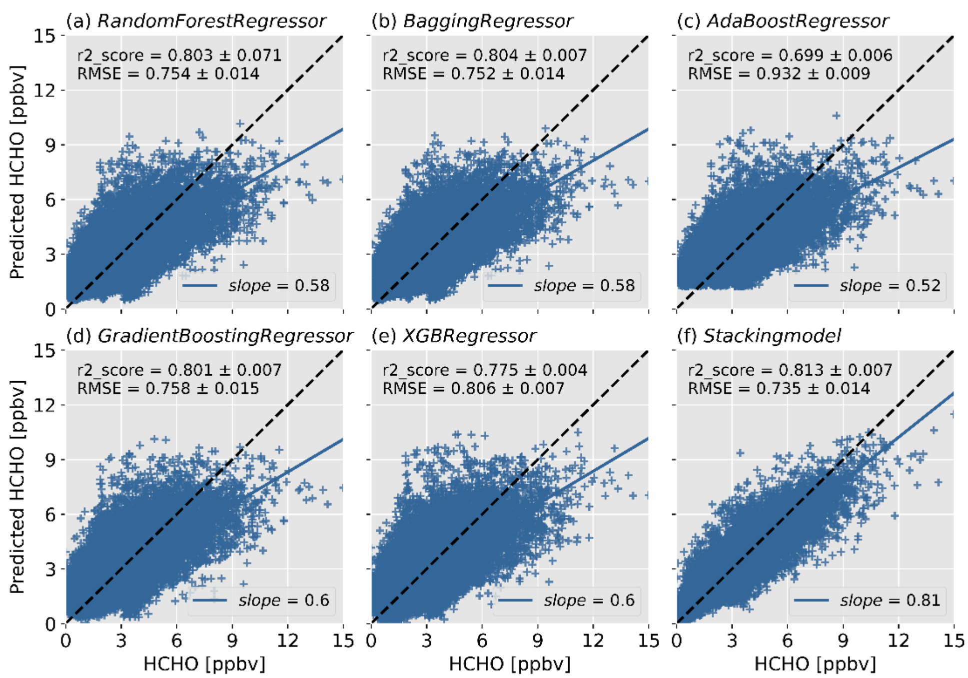

Figure S4. Performance comparisons of the stacking model and the five base models after 5-fold cross-validation with the indicators of r2_score, RMSE, and slope between predicted and measured HCHO.

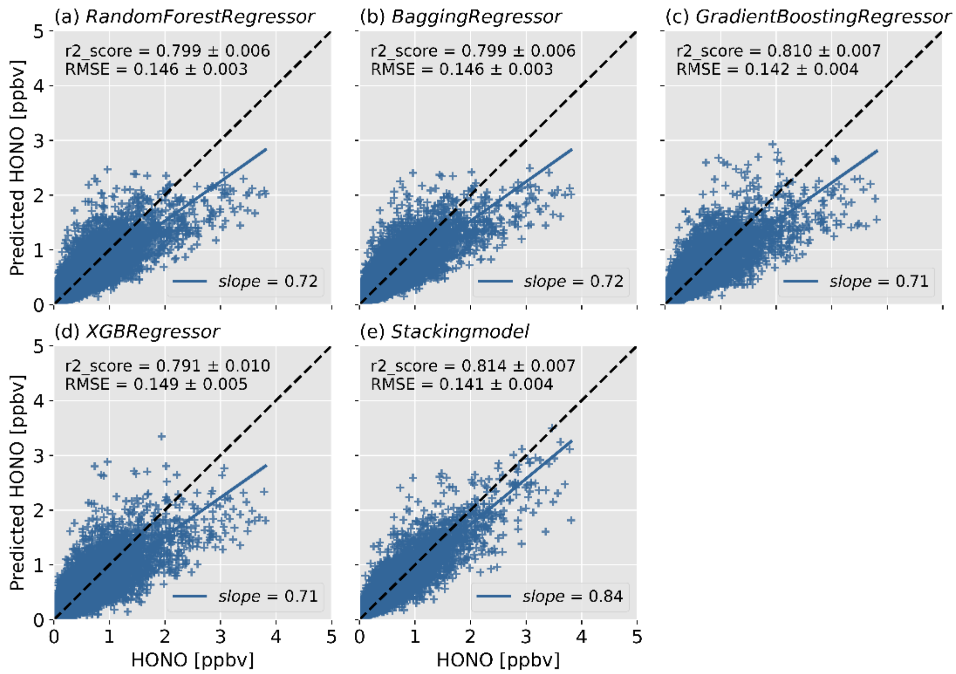

Figure S5. Performance comparisons of the stacking model and the four base models after 5-fold cross-validation with the indicators of r2_score, RMSE, and slope between predicted and measured HONO.

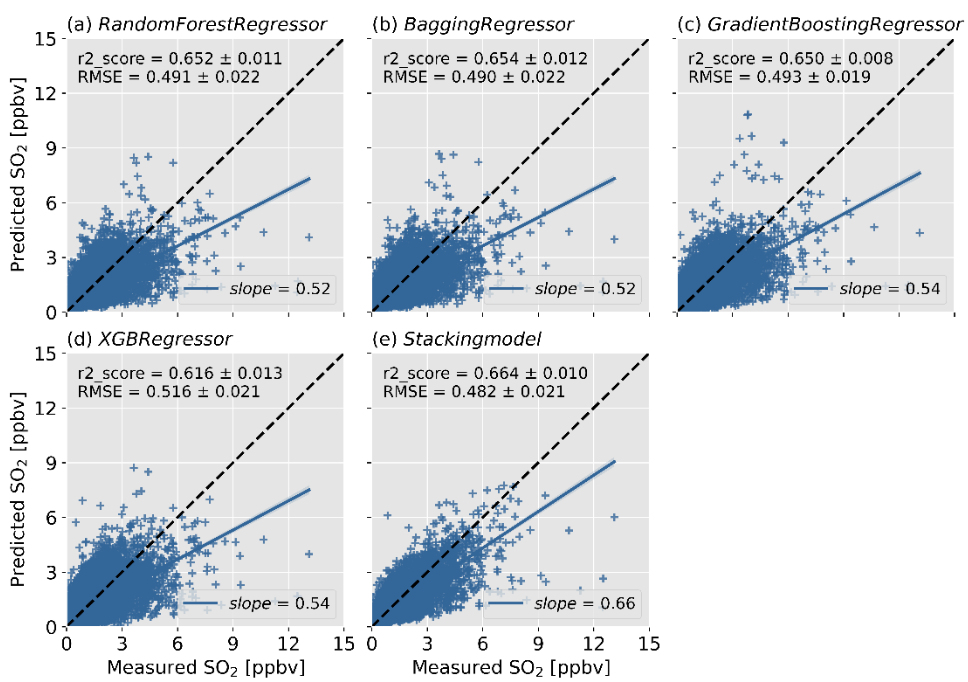

Figure S6. Performance comparisons of the stacking model and the four base models after 5-fold cross-validation with the indicators of r2_score, RMSE, and slope between predicted and measured SO_2.

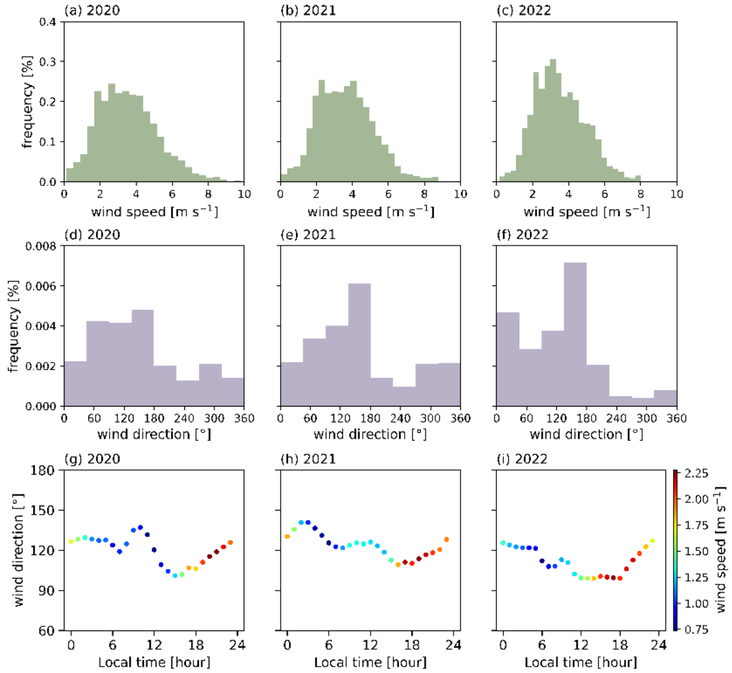

Figure S7. The frequency (a-f) and the mean diurnal profiles (d, h, i) of wind speed and wind direction during the periods from April to May of 2020, 2021, and 2022.

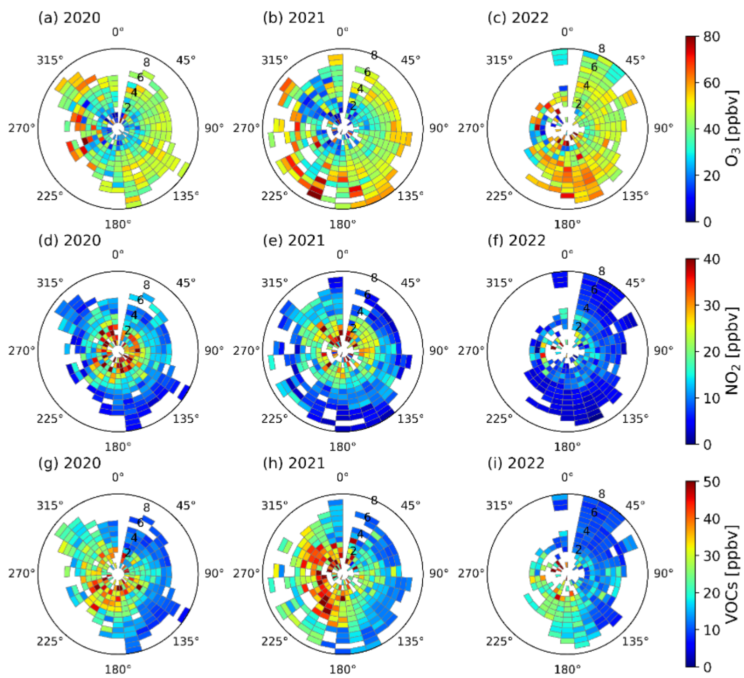

Figure S8. The polar plots of O_3 (a, b, c), NO_2 (d, e, f) and VOCs (g, h, i) during the periods from April to May of 2020, 2021, and 2022.

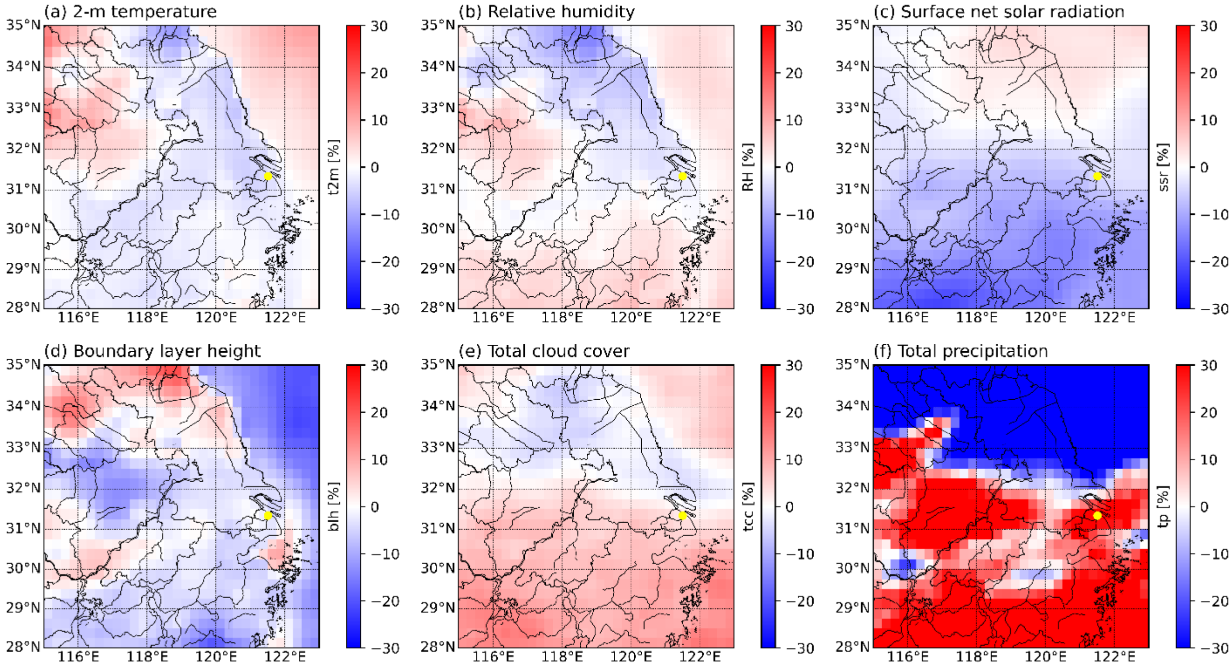

Figure S9. The percentage change in average meteorological parameters from the ERA5 data for Shanghai and its neighboring regions during the 2022 lockdown period compared to the same period in 2020. The 2-m temperature (t2m) (a), relative humidity calculated based on 2-m temperature and 2-m dewpoint temperature (b), surface net solar radiation (ssr) (c), boundary layer height (blh) (d), total cloud cover (tcc) (e), and total precipitation (tp) (f).

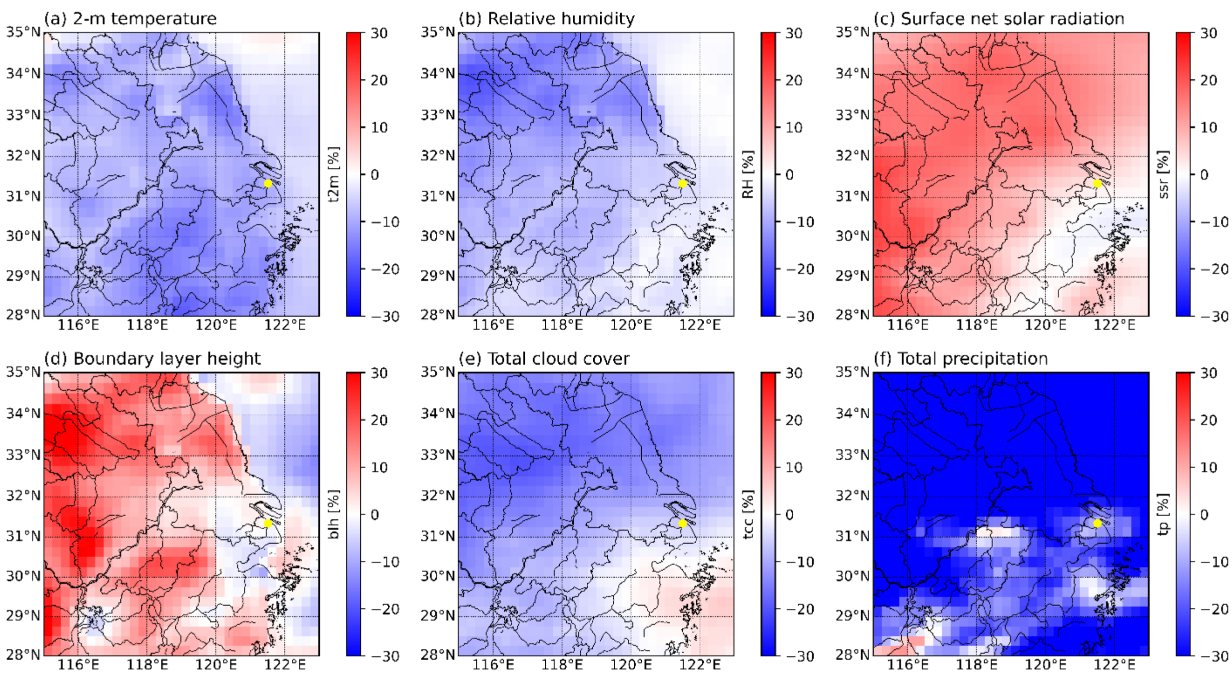

Figure S10. Same as Figure S9 but compared to the same period in 2021.

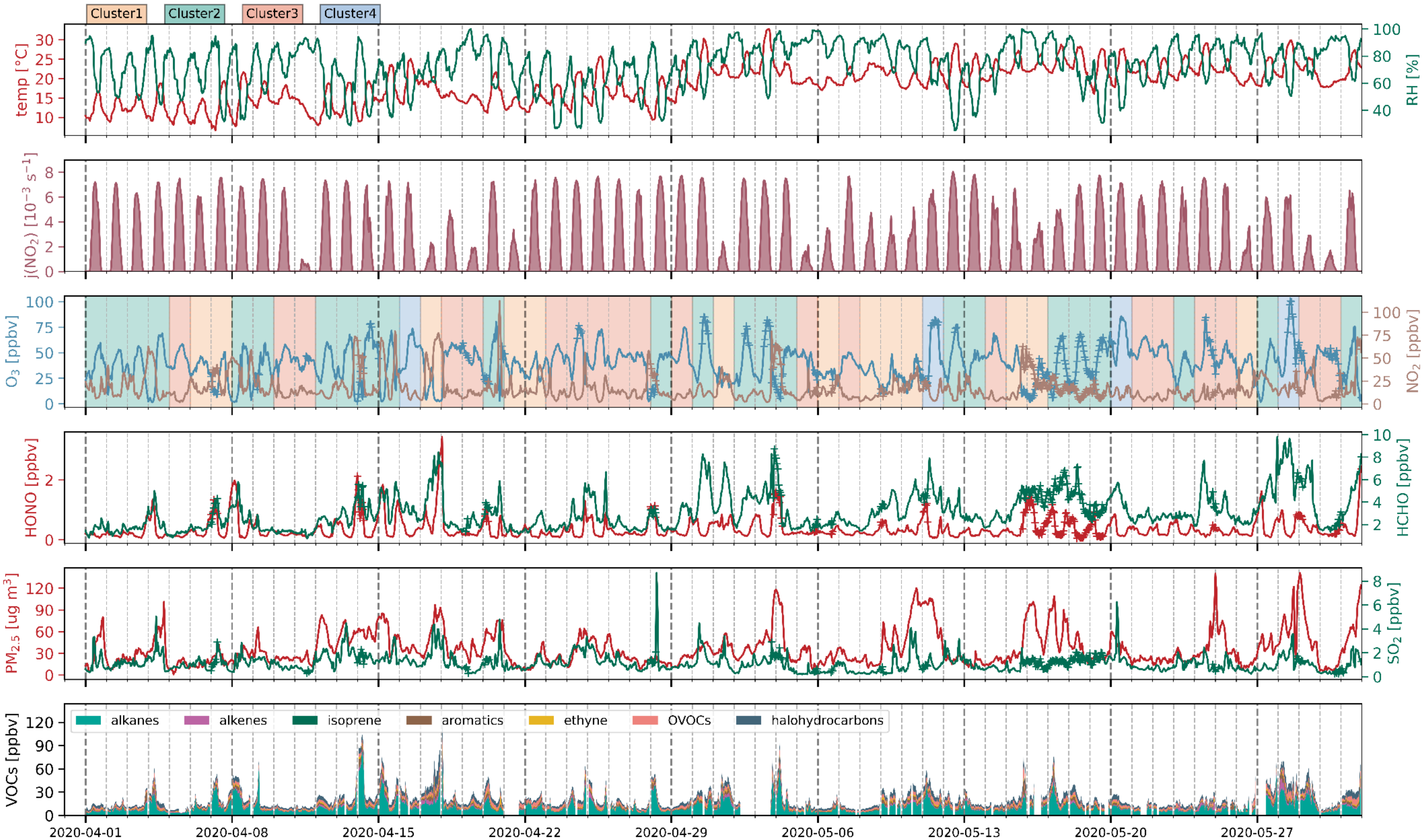

Figure S11. Time series of meteorological parameters (temp, RH, *j*(NO_2)) and air pollutants (O_3, NO_2, HONO, HCHO, SO_2, $PM_{2.5}$, VOCs) from April to May 2020. The data with the "+" symbol represents the predictions made by machine learning and is used to fill in missing values in the observations.

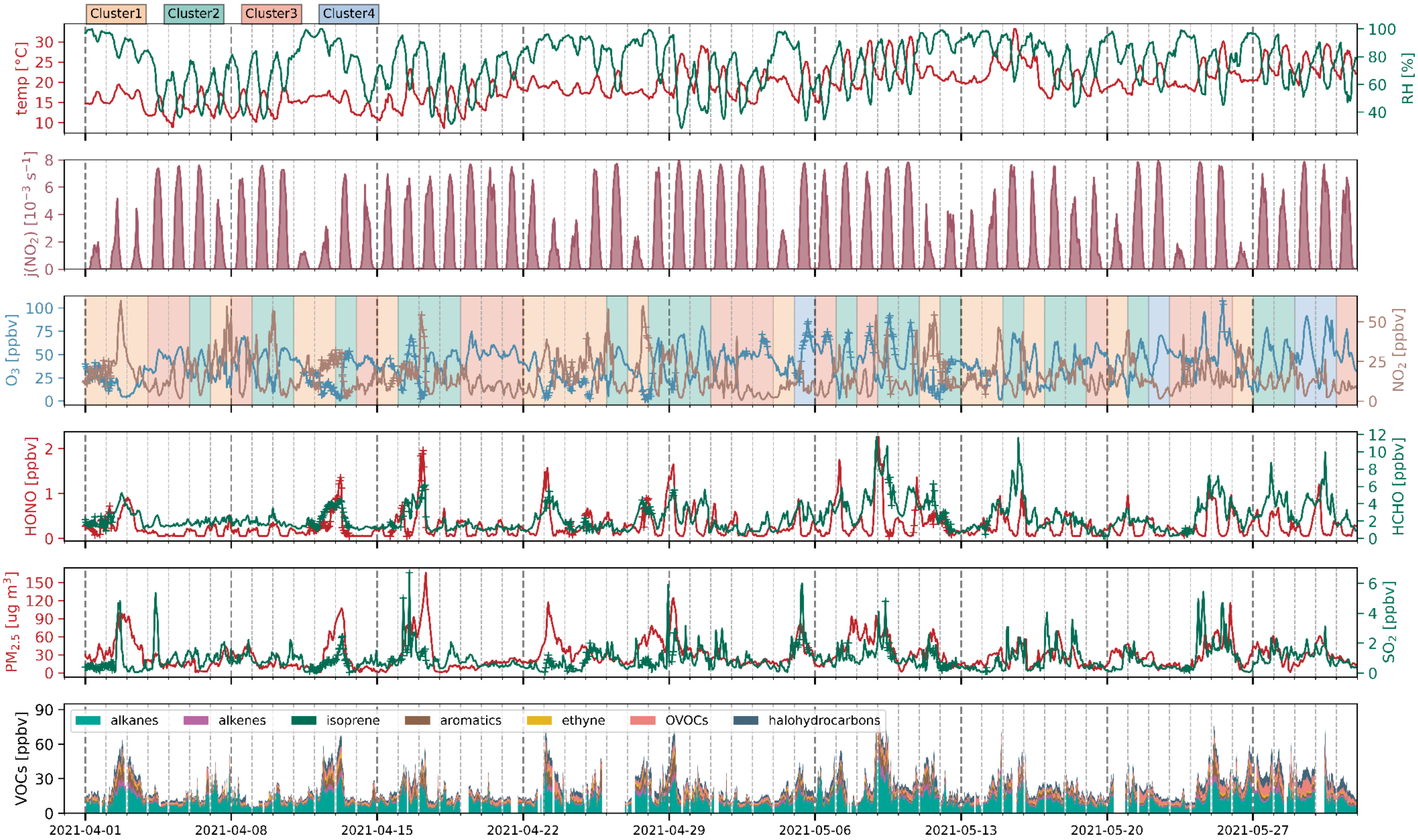

Figure S12. Same as Figure S11, but for the period between April and May 2021.

Figure S13. Same as Figure S11, but for the period between April and May 2022.

Table S1. The configuration of spectral fitting of O_3, NO_2, SO_2, HONO and HCHO.

Trace gas	Fitting window (nm)	absorption cross sections	Polynomial degree	detection limits
O_3	280.6-290.6	O_3 (Voigt et al., 2001), SO_2 (Vandaele et al., 2009), HCHO (Meller and Moortgat, 2000), and NO_2 (Voight et al., 2002)	5	1.3 ppbv
NO_2	365.3-380.4	NO_2 (Voight et al., 2002), HONO (Stutz et al., 2000), HCHO (Meller and Moortgat, 2000), and solar spectrum (Kurucz, 1984)	5	0.5 ppbv
SO_2	295.3-307.9	SO_2 (Vandaele et al., 2009), O_3 (Voigt et al., 2001), HCHO (Meller and Moortgat, 2000), NO_2 (Voight et al., 2002), and solar spectrum (Kurucz, 1984)	5	0.1 ppbv
HONO	339.4-373.2	HONO (Stutz et al., 2000), NO_2 (Voight et al., 2002), HCHO (Meller and Moortgat, 2000), and solar spectrum (Kurucz, 1984)	5	0.1 ppbv
HCHO	311.7-342.1	HCHO (Meller and Moortgat, 2000), NO_2 (Voight et al., 2002), HONO (Stutz et al., 2000), O_3 (Voigt et al., 2001), SO_2 (Vandaele et al., 2009) , and solar spectrum (Kurucz, 1984)	5	0.5 ppbv

Table S2. Summary of the mean concentration of measured VOCs during the periods from April to May of 2020, 2021, and 2022.

Species	Average concentration (mean ± std, unit: ppbv)		
alkanes	**2020**	**2021**	**2022**
Ethane	4.36 ± 3.73	4.30 ± 2.02	3.66 ± 2.57
Propane	2.91 ± 2.91	2.96 ± 1.96	1.63 ± 1.28
n-Butane	1.12 ± 1.04	1.23 ± 0.87	0.70 ± 0.67
Isobutane	0.86 ± 0.96	1.00 ± 0.83	0.54 ± 0.53
n-Pentane	0.46 ± 0.55	0.50 ± 0.44	0.32 ± 0.34
Isopentane	0.82 ± 1.07	0.92 ± 0.99	0.66 ± 0.83
Cyclopentane	0.04 ± 0.04	0.04 ± 0.07	0.03 ± 0.04
n-Hexane	0.13 ± 0.16	0.14 ± 0.15	0.06 ± 0.06
2,2-Dimethylbutane	0.02 ± 0.03	0.03 ± 0.02	0.01 ± 0.01
Cyclohexane	0.05 ± 0.07	0.05 ± 0.07	0.02 ± 0.02
2,3-Dimethylbutane	0.03 ± 0.03	0.05 ± 0.04	
2-Methylpentane	0.15 ± 0.16	0.21 ± 0.19	0.09 ± 0.09
3-Methylpentane	0.12 ± 0.14	0.11 ± 0.12	0.04 ± 0.06
Methylcyclopentane	0.04 ± 0.04	0.05 ± 0.04	0.02 ± 0.02
n-Heptane	0.04 ± 0.04	0.05 ± 0.06	0.02 ± 0.03
2,3-Dimethylpentane	0.01 ± 0.01	0.02 ± 0.02	0.00 ± 0.01
2,4-Dimethylpentane	0.01 ± 0.01	0.01 ± 0.01	0.00 ± 0.00
3-Methylhexane	0.03 ± 0.03	0.04 ± 0.04	0.02 ± 0.02
2-Methylhexane	0.03 ± 0.02	0.03 ± 0.03	0.01 ± 0.01
Methylcyclohexane	0.03 ± 0.04	0.04 ± 0.05	0.02 ± 0.02
n-Octane	0.04 ± 0.05	0.03 ± 0.03	0.01 ± 0.01
2,2,4-trimethylpentane	0.02 ± 0.02	0.02 ± 0.02	0.00 ± 0.01
2,3,4-trimethylpentane	0.01 ± 0.01	0.01 ± 0.01	0.00 ± 0.01
2-Methylheptane	0.01 ± 0.01	0.01 ± 0.01	0.01 ± 0.01
3-Methylheptane	0.01 ± 0.01	0.01 ± 0.01	0.00 ± 0.01
n-nonane	0.02 ± 0.02	0.02 ± 0.01	0.01 ± 0.01
n-Decane	0.02 ± 0.01	0.02 ± 0.02	0.00 ± 0.01
n-undecane	0.01 ± 0.01	0.02 ± 0.01	0.00 ± 0.01
n-Dodecane	0.02 ± 0.01	0.02 ± 0.01	0.20 ± 0.36

alkenes			
Ethylene	0.91 ± 1.14	1.13 ± 1.06	0.60 ± 0.61
Propylene	0.26 ± 0.50	0.30 ± 0.36	0.30 ± 0.83
Isobutylene	0.04 ± 0.05	0.06 ± 0.04	0.04 ± 0.03
1-butene	0.06 ± 0.09	0.08 ± 0.08	0.06 ± 0.08
cis-2-butene	0.03 ± 0.04	0.13 ± 0.06	0.05 ± 0.03
trans-2-butene	0.02 ± 0.05	0.05 ± 0.07	0.03 ± 0.05
1,3-Butadiene	0.01 ± 0.04	0.02 ± 0.02	0.01 ± 0.04
1-pentene	0.02 ± 0.02	0.04 ± 0.03	0.02 ± 0.01
cis-2-pentene	0.00 ± 0.01	0.00 ± 0.01	0.00 ± 0.00
trans-2-pentene	0.00 ± 0.03	0.00 ± 0.01	0.00 ± 0.01
1-Hexene	0.01 ± 0.01	0.00 ± 0.01	0.00 ± 0.00
isoprene	0.04 ± 0.09	0.06 ± 0.11	0.03 ± 0.06
Alkyne			
Acetylene	0.96 ± 0.69	1.14 ± 0.78	0.75 ± 0.38
aromatic			
Benzene	0.34 ± 0.25	0.40 ± 0.38	0.24 ± 0.20
Toluene	0.57 ± 0.67	0.92 ± 1.56	0.18 ± 0.23
Ethylbenzene	0.20 ± 0.26	0.27 ± 0.39	0.05 ± 0.05
o-Xylene	0.16 ± 0.26	0.22 ± 0.34	0.04 ± 0.05
m-Xylene	0.28 ± 0.43	0.40 ± 0.58	0.06 ± 0.08
p-xylene	0.28 ± 0.43	0.40 ± 0.58	0.06 ± 0.08
Styrene	0.02 ± 0.03	0.03 ± 0.05	0.00 ± 0.01
1,2,3-Trimethylbenzene	0.01 ± 0.01	0.01 ± 0.01	0.00 ± 0.00
1,2,4-Trimethylbenzene	0.04 ± 0.05	0.04 ± 0.04	0.01 ± 0.01
1,3,5-Trimethylbenzene	0.01 ± 0.02	0.01 ± 0.02	0.00 ± 0.00
o-Ethyl toluene	0.01 ± 0.01	0.02 ± 0.01	0.00 ± 0.01
m-Ethyltoluene	0.02 ± 0.03	0.03 ± 0.03	0.01 ± 0.01
p-Ethyltoluene	0.01 ± 0.02	0.02 ± 0.02	0.00 ± 0.00
Isopropylbenzene	0.01 ± 0.01	0.01 ± 0.01	0.00 ± 0.01
n-propylbenzene	0.01 ± 0.01	0.01 ± 0.01	0.00 ± 0.00
m-diethylbenzene	0.00 ± 0.01	0.00 ± 0.00	0.00 ± 0.00
p-diethylbenzene	0.01 ± 0.01	0.01 ± 0.01	0.00 ± 0.00
OVOCs			
Acetone	1.81 ± 1.40	2.53 ± 2.08	1.94 ± 0.98
Propionaldehyde	0.17 ± 0.10	0.13 ± 0.11	0.11 ± 0.05
Acrolein	0.07 ± 0.06	0.05 ± 0.04	0.03 ± 0.02
2-Butanone	0.03 ± 0.02	0.03 ± 0.02	0.04 ± 0.02
Butyraldehyde	0.03 ± 0.02	0.03 ± 0.02	0.04 ± 0.02
2-Methylacrylaldehyde	0.03 ± 0.05	0.03 ± 0.04	0.01 ± 0.02
Methyl tert-butyl ether	0.22 ± 0.33	0.14 ± 0.16	0.07 ± 0.12
3-Pentanone	0.02 ± 0.01	0.01 ± 0.01	0.01 ± 0.01
Valeraldehyde	0.03 ± 0.02	0.03 ± 0.01	0.02 ± 0.02
2-Pentanone	0.02 ± 0.01	0.01 ± 0.01	0.02 ± 0.01
Benzyl chloride	0.00 ± 0.01	0.00 ± 0.00	0.00 ± 0.00
Hexanal	0.37 ± 0.37	0.24 ± 0.27	0.32 ± 0.35
Methyl vinyl ketone(butenone)	0.05 ± 0.06	0.03 ± 0.05	0.02 ± 0.02
halohydrocarbons			
Chloromethane	1.24 ± 0.81	0.64 ± 0.30	0.80 ± 0.25

Dichloromethane	1.16 ± 1.34	1.27 ± 1.11	0.57 ± 0.46
Chloroform	0.13 ± 0.17	0.11 ± 0.08	0.06 ± 0.03
Carbon tetrachloride	0.12 ± 0.03	0.10 ± 0.02	0.13 ± 0.02
Bromomethane	0.03 ± 0.04	0.02 ± 0.02	0.02 ± 0.01
Bromoform	0.01 ± 0.01	0.01 ± 0.01	0.00 ± 0.01
Monobromodichloromethane	0.00 ± 0.00	0.00 ± 0.00	0.00 ± 0.00
Trichloromonofluoromethane	0.53 ± 0.16	0.80 ± 0.88	0.58 ± 0.21
Chloroethane	0.05 ± 0.11	0.05 ± 0.10	0.02 ± 0.03
1,1-Dichloroethane	0.01 ± 0.01	0.01 ± 0.01	0.00 ± 0.01
1,2-Dichloroethane	0.41 ± 0.39	0.34 ± 0.29	0.20 ± 0.15
1,1,1-Trichloroethane	0.00 ± 0.00	0.00 ± 0.00	0.00 ± 0.00
1,1,2-Trichloroethane	0.03 ± 0.03	0.02 ± 0.02	0.01 ± 0.01
1,1,2,2-Tetrachloroethane	0.00 ± 0.01	0.00 ± 0.00	0.00 ± 0.00
1,2-dibromoethane	0.00 ± 0.00	0.00 ± 0.00	0.00 ± 0.00
Dichlorotetrafluoroethane	0.02 ± 0.01	0.02 ± 0.01	0.02 ± 0.00
Trichlorotrifluoroethane	0.10 ± 0.02	0.07 ± 0.02	0.07 ± 0.00
Vinyl chloride	0.02 ± 0.04	0.01 ± 0.04	0.00 ± 0.01
1,1-Dichloroethylene	0.00 ± 0.01	0.00 ± 0.01	0.00 ± 0.00
cis-1,2-dichloroethylene	0.00 ± 0.00	0.00 ± 0.00	0.00 ± 0.00
Trichloroethylene	0.04 ± 0.07	0.03 ± 0.05	0.01 ± 0.01
Tetrachloroethylene	0.04 ± 0.04	0.04 ± 0.04	0.02 ± 0.02
1,2-Dichloropropane	0.06 ± 0.06	0.10 ± 0.11	0.05 ± 0.06
cis-1,3-dichloropropene	0.00 ± 0.00	0.00 ± 0.00	0.00 ± 0.00
trans-1,3-dichloropropene	0.00 ± 0.00	0.00 ± 0.00	0.00 ± 0.00
Chlorobenzene	0.02 ± 0.02	0.01 ± 0.03	0.00 ± 0.01
1,2-Dichlorobenzene	0.01 ± 0.01	0.01 ± 0.01	0.00 ± 0.00
1,3-Dichlorobenzene	0.00 ± 0.01	0.00 ± 0.01	0.00 ± 0.00
1,4-Dichlorobenzene	0.04 ± 0.05	0.04 ± 0.04	0.02 ± 0.03
Iodomethane	0.00 ± 0.00	0.00 ± 0.00	0.00 ± 0.00
Acetonitrile	0.10 ± 0.10	0.13 ± 0.10	0.14 ± 0.08

References:

Kurucz, R. L.: Solar Flux Atlas from 296 to 1300 nm, National Solar Observatory Atlas, 1, https://doi.org/10.1017/S0074180900035427, 1984.

Meller, R. and Moortgat, G. K.: Temperature dependence of the absorption cross sections of formaldehyde between 223 and 323 K in the wavelength range 225-375 nm, Journal of Geophysical Research: Atmospheres, 105, 7089-7101, https://doi.org/10.1029/1999JD901074, 2000.

Stutz, J., Kim, E., Platt, U., Bruno, P., Perrino, C., and Febo, A.: UV - visible absorption cross sections of nitrous acid, Journal of Geophysical Research: Atmospheres, 105, 14585-14592, https://doi.org/10.1029/2000JD900003, 2000.

Vandaele, A. C., Hermans, C., and Fally, S.: Fourier transform measurements of SO_2 absorption cross sections: II.: Temperature dependence in the 29000-44000 cm^{-1} (227-345 nm) region, Journal of Quantitative Spectroscopy and Radiative Transfer, 110, 2115-2126, https://doi.org/10.1016/j.jqsrt.2009.05.006, 2009.

Voight, S., Orphal, J., and Burrows, J.: The temperature and pressure dependence of the absorption cross-sections of NO_2 in the 250-800 nm region measured by Fourier-transform spectroscopy, Journal of

Photochemistry and Photobiology A: Chemistry, 149, 1-7, https://doi.org/10.1016/s1010-6030(01)00650-5, 2002.

Voigt, S., Orphal, J., Bogumil, K., and Burrows, J.: The temperature dependence (203-293 K) of the absorption cross sections of O_3 in the 230-850 nm region measured by Fourier-transform spectroscopy, Journal of Photochemistry and Photobiology A: Chemistry, 143, 1-9, https://doi.org/10.1016/S1010-6030(01)00480-4, 2001.